Optimal Mass, Spin, and Orientation Parameters for Detecting Higher Order Gravitational-wave Modes from Binary Black Hole Mergers

Mahlet Shiferaw*
Harvard-Smithsonian Center for Astrophysics, Cambridge, MA 02138

Mentors: Alan Weinstein† and Liting Xiao‡
LIGO, California Institute of Technology, Pasadena, CA 91125

(LIGO Collaboration)

(Dated: October 15, 2019)

Thus far, the Advanced Laser Interferometer Gravitational-Wave Observatory (aLIGO) and Advanced Virgo have detected gravitational waves (GWs), or ripples in the curvature of spacetime, from dozens of binary black hole (BBH) and binary neutron star mergers. In order to detect these GWs, aLIGO data are optimally searched against a bank of model waveform templates well-described by General Relativity (GR). These searches only include waveforms for the dominant $\ell = 2, m = 2$ mode, neglecting higher order modes (HOMs) which carry important information about the source and its radiation. Furthermore, HOMs are lower in amplitude than the dominant mode, and tend to lie outside of aLIGO's sensitive frequency band for low-mass systems, making their detection very unlikely. Constrained by this strain sensitivity, we use waveforms produced by numerical relativity simulations to assess the capabilities of aLIGO for detecting HOMs, thus paving the way for a powerful test of GR in the strong-field highly dynamical regime. To determine the range of BBH mass, spin, and orbital orientations which optimizes the likelihood of detecting HOM, we therefore calculate the overlap integral between templates with and without HOMs, as well as the maximum effective luminosity distance to the source. Within a range of assumptions discussed in this paper, we find the following results: the total mass and mass ratio of the merger should be as large as possible, and the aligned spin should be as large and positive as possible. We find the relationship with inclination angle to be more complicated, as it depends on which combination of HOMs are most dominant at a certain mass ratio.

Usage: Caltech SURF Final Report.

I. INTRODUCTION

Gravitational waves (GWs) are violent ripples of spacetime created by catastrophic events such as merging black hole binaries, supernovae, and colliding neutron star binaries. Predicted by physicist Albert Einstein in his Theory of General Relativity (GR) in 1915, Einstein's field equations show that such massive accelerating objects cause distorted waves to travel through the fabric of spacetime at the speed of light [1, 2].

Despite this breakthrough, GWs were not detected for another century, until September 14th, 2015, when the two detectors of the Advanced Laser Interferometer Gravitational-Wave Observatory (aLIGO) both observed the first GW signal, GW150914, at 09:50:45.4 UTC [3]. Caused by a binary black hole (BBH) merger, GW150914 was detected during the first observing run (O1) of Advanced LIGO, which ran from September 12th, 2015 to January 19th, 2016 [4]. The second observing run (O2) ran from November 30th, 2016 to August 25th, 2017, and on August 1st, 2017, the Advanced Virgo detector joined O2, allowing for three detectors to simultaneously search for GWs for the first time in history [5].

aLIGO is the world's largest, most complex, and most sensitive interferometer, designed purely for the detection of these miniscule oscillations in spacetime. Soon, a global network of detectors will join aLIGO, with three detectors having already been built in Japan, Italy, and Germany [6], and a third LIGO detector to be built in India. Furthermore, the third observing run (O3) of Advanced LIGO and Virgo began in April 2019, and is planned to continue throughout the summer of 2019 for one calender year [7]. As such, gravitational waves are ushering in a new era of multi-messenger astronomy, in which astrophysicists have an entirely new way of viewing and understanding the cosmos.

A. Detection of Gravitational Waves

These developments represent an exciting opportunity to take advantage of the increased number of detections and enhanced signal-to-noise ratio (SNR), both of which will presumably only increase as the years go by. The implications of these improvements are numerous, as GWs carry not just energy and momentum, but crucial infor-

* mshiferaw@college.harvard.edu
† ajw@caltech.edu
‡ lxxiao@caltech.edu

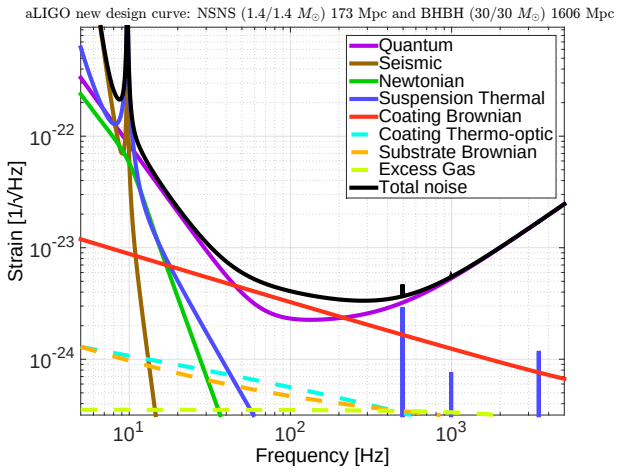

FIG. 1. The updated aLIGO design curve, which takes into account coating thermal noise. In black is the total noise of the design curve. Figure courtesy of LIGO Scientific Collaboration.

mation about the structure of their sources. In particular, a quasi-circular coalescing compact binary is completely characterized by fifteen parameters, which include the mass of each object in the merger, their spins, and their orbital orientation [8].

During an observing run, aLIGO continually takes in data, which means that these data must simultaneously be scrutinized for possible GW events. Events are thus detected using a technique called matched filtering, which selects the optimal model waveform for an observed signal from a collection of waveforms called a template bank. Because the key parameters which describe a waveform, such as the amplitude, masses, spins, fiducial reference time, and orbital phase, are not known before matched filtering begins, such template banks search through parameter space to construct thousands of possible gravitational waveforms [9].

Matched filtering is used to search the data for resemblance to each template for each time step dt of data. If a time step has an SNR $\gtrapprox 8$, further investigations are done using Bayesian inference, a process which takes the model waveform and, given a range of parameters and expectations for noise, produces posterior distributions on the input parameters. With this, refined parameters can be extracted from any signal with a high enough SNR.

B. Higher Order Modes

During matched filtering, current model waveforms are restricted so that they only include the leading order Y_{22} mode of the waveform. This is because the full waveform, which includes the sum of all modes, depends on the viewing angle of the observer, something that is not known at the time of the search. This restriction, while providing reasonable estimations at a far less computationally expensive rate, comes at a cost: as both Payne et al. [10] and Kumar et al. [11] have shown, including HOMs provides tighter constraints on the source parameters than the fundamental $\ell = 2$ mode.

This has three main benefits: including HOMs in our calculations will allow this parameter estimation procedure to become much more precise, thus greatly furthering our understanding of these GW sources. Furthermore, using waveforms with HOMs will likely increase the similarities between template and data during matched filtering, thus boosting aLIGO's detection confidence. Finally, including HOMs makes it possible to test for their presence in the signal found in the data, a powerful test of GR as the theory of strong gravity and GWs.

Unfortunately, there is yet another difficulty in including these HOMs in the parameter estimation process. HOMs are at least half an order of magnitude fainter than the dominant Y_{22} mode, and for low-mass systems, tend to lie outside of the total noise curve in aLIGO's sensitivity frequency band, depicted in Figure 1. This has a two-fold effect in both parameter estimation and matched filtering: this means that no HOMs have been detected yet, and will likely not be detected until either aLIGO's sensitivies improve or a detector happens to observe a close-by event with high SNR. As a result, in this project we aim to determine exactly how high in SNR an event detection needs to be in order to present statistically significant evidence for HOMs. In assessing the full extent of aLIGO's capabilities for detecting these HOMs, we will be able to better inform future detections, especially as aLIGO continues to be upgraded.

We will accomplish this by first computing the ratio of SNR for templates with and without HOMs, using a surrogate model for hybridized nonprecessing numerical relativity waveforms called `NRHybSur3dq8` [12]. We will maximize this ratio for a range of input parameters, allowing us to determine optimal range of source merger mass, spin, and orbital orientation for detecting HOMs as constrained by aLIGO's total noise. Finally, we will calculate the maximum effective luminosity distance to the source which will allow aLIGO to detect this difference in SNR. Because HOMs are predicted by GR but have not yet been detected, this will also allow us to perform unique and powerful tests on GR in the strong-field, highly dynamical regime.

This paper is organized as follows: in Section II, we outline the relevant equations used in computing the strain of a gravitational wave signal. In Section III, we outline the methods used in answering our research question on he detectability of higher order modes. We begin in Section III A by computing the strain emitted by the source merger and visualizing the resulting waveform. In Section III B, we use the antenna response of the detector in order to calculate the strain that the detector observes in the time-domain. In Section III C, we prepare the data so that it is fit for a Fourier Transform into the frequency domain, which we perform in Section III D.

We then compare this frequency-domain data to the updated aLIGO design curve pictured in 1, and visualize the instantaneous peak frequency. Finally we are able to compute the overlap integral and luminosity distance in Section III E. In Section IV and V, we show and discuss the results of our findings.

II. RELEVANT EQUATIONS

In this section, we outline relevant equations for the dominant Y_{22} mode of a gravitational waveform during the inspiral phase. The characteristic dimensionless gravitational wave strain amplitude h for a source of mass M located at a distance r away can be described by Equation 1. In this notation, Q refers to the quadrupole moment of the source event, ω is its angular frequency of orbit, μ is the reduced mass, a is the instantaneous separation between the two source frame component masses m_1 and m_2, and M is the total mass of the merger [13]:

$$h \sim \frac{G}{c^4}\frac{1}{r}\frac{d^2Q}{dt^2}, \quad \frac{d^2Q}{dt^2} = -\omega^2\mu a^2, \quad \mu = \frac{m_1 m_2}{M} = \frac{m_1 m_2}{m_1 + m_2} \tag{1}$$

The angular frequency ω can be rewritten in terms of the orbital period, using Kepler's third law in Equation 2:

$$\omega = 2\pi f_{\rm orb} = \frac{2\pi}{\tau_{\rm orb}}, \quad {\tau_{\rm orb}}^2 = \frac{4\pi^2}{G(m_1+m_2)}a^3 = \frac{4\pi^2}{GM}a^3 \tag{2}$$

Here, $f_{\rm GW} = 2f_{\rm orb}$, where $f_{\rm GW}$ refers to the frequency of the gravitational wave in the $\ell = 2, m = 2$ mode and $f_{\rm orb}$ is the orbital frequency. Equation 1 can thus be rewritten as Equation 3, where $R_{\rm S}$ is the Schwarzschild radius of the source and η is the dimensionless mass factor:

$$h \sim -\frac{GM}{c^2 r}\frac{G\mu}{c^2 a} \sim -\frac{\eta {R_{\rm S}}^2}{4ra} \tag{3a}$$

$$\eta = \frac{\mu}{M} = \frac{m_1 m_2}{M^2}, \quad R_{\rm S} = \frac{2GM}{c^2} \tag{3b}$$

The strain amplitude in Equation 3a can also be written in terms of the chirp mass $\mathcal{M}$, as defined by Equation 4 below:

$$h(t) \sim -\frac{1}{c^4 r}(G^5\mathcal{M}^5\pi^2 f_{\rm GW}^2(t))^{1/3}, \quad \mathcal{M} = M\,\eta^{3/5} \tag{4}$$

From these equations, it is clear that GWs can inform us about many features of the source event. Source parameters from newly detected GWs can thus be extracted using Bayesian parameter estimation, a method of extracting the correct parameters for mathematical models of physical systems. In contrast to the classical frequentist approach, which chooses a value for some input parameter θ that maximizes the likelihood of the observed data, Bayesian parameter estimation holds the observed evidence as fixed and instead infers a Posterior Density Function (PDF) for θ [14]. Bayesian inference is a crucial tool in all of modern science, but is particularly useful in gravitational wave astronomy, as a black hole can be completely characterized by its mass and spin vector, and the gravitational waveform from a BBH by a total of fifteen parameters [15]. These are composed of the following intrinsic parameters:

(1) the source frame component BH masses m_1 and m_2;

(2) the component BH spin vectors $\vec{\chi}_1$ and $\vec{\chi}_2$;

as well as the following extrinsic parameters:

(3) the luminosity distance d_L;

(4) the source's sky location $\Delta\Omega$, characterized by its right ascension (RA) and right declination (Dec);

(5) the polar angle ι and polarization angle ψ of the orientation of the binary orbit with respect to the line-of-sight of the observer;

(6) the coalescence time t_c at which the signal from the merger reaches the center of the Earth;

(7) the phase of the signal ϕ_c at the moment of coalescence.

The observer's viewing angle to the source ι is a key parameter which differentiates the full waveform from the restricted waveform. In the latter case, it is an extrinsic parameter, meaning that only the overall amplitude is dependent on it. In contrast, for the full waveform with HOMs, ι becomes an intrinsic parameter upon which the shape of the waveform is also dependent.

There are a number of other parameters which can be derived from these fifteen input parameters, including the final source frame mass M_f, the final spin a_f, the radiated energy $E_{\rm rad}$, the peak luminosity $l_{\rm peak}$, the redshift z, the chirp mass $\mathcal{M}$, and the dimensionless effective aligned spin $\chi_{\rm eff}$. The latter is described by Equation 5, where $\hat{L}_N$ is the orbital angular momentum of the source event:

$$\chi_{\rm eff} = \frac{(m_1\vec{\chi}_1 + m_2\vec{\chi}_2)\cdot\hat{L}_N}{M} \tag{5}$$

III. METHODS

This project requires the use of `NRHybSur3dq8`, a surrogate model for hybridized nonprecessing numerical relativity waveforms which includes modes $\ell = 2$ through

Parameter	Value
Approximant	`NRHybSur3dq8`
Timestep	1/4096 s
Distance	100 Mpc
Mass Ratio, q	1
Aligned Spin $\chi_{1,z}$	0.5
Aligned Spin $\chi_{2,z}$	0
Total Mass, M	100 $M_\odot$
Inclination, ι	π
Azimuthal Angle, ϕ	0
Initial Frequency	10 Hz

TABLE I. Parameters for the individual waveform plotted in Figures 2 through 7. We have chosen a frequency of 4096 Hz because it is twice the Nyquist frequency, and $\chi_{1,z}$ and $\chi_{2,z}$ are the aligned spin of the larger and smaller components of the merger, respectively.

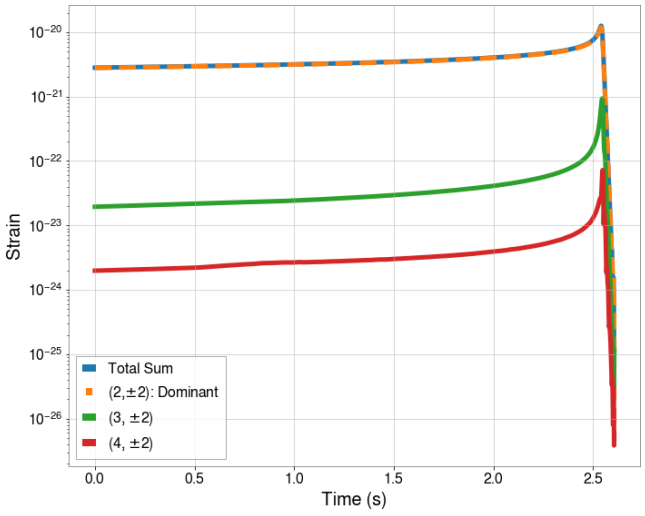

FIG. 2. The real strain amplitude of the fundamental Y_{22} mode for a numerical relativity surrogate waveform is plotted in orange, along with two of the strongest HOMs. Here it becomes clear that HOMs are many orders of magnitude weaker in amplitude than the dominant mode, due to the fact that the mass ratio $q = 1$. Plotted in blue is the full waveform, or the total sum of all modes, which oscillates in time due to orbital precession. The merger is given the parameters listed in Table I.

$\ell = 4$, as well as the Y_{55} mode. In addition to these numerical relativity waveforms, we use the `GWpy` software package in Python [16]. Our approach consists of first visualizing a waveform for just one instance of an event with and without HOMs, and then generalizing to all events across many masses, spins and orbital inclinations in order to find the range of initial parameters that will maximize aLIGO's chances of detecting HOMs.

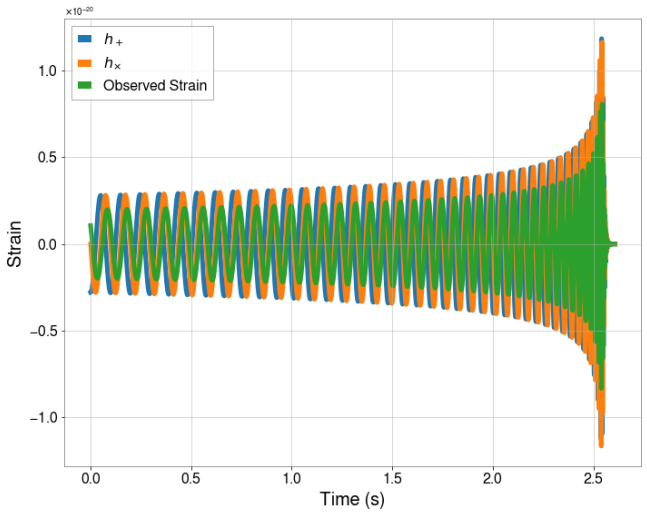

FIG. 3. The real and imaginary portions of the strain are plotted in blue and orange, respectively. Plotted in green is what a detector would observe given its antenna response.

A. Visualizing the Waveform

In order to fully investigate HOMs, we must first gain a physical intuition for how the full waveform behaves in comparison to the dominant mode, as well as each of the individual HOMs. We accomplish this through visualizing the waveform generated by a numerical relativity surrogate model with the parameters listed in Table I. In this model, the strain is represented as a complex number with the imaginary part corresponding to the cross polarization, and the real part to the plus polarization.

Using this convention, in Figure 2, we plot the absolute value of the strain for the dominant Y_{22} mode, as well as two of the strongest HOMs, on a semi-log scale. Although the phase evolution for (ℓ, m) and $(\ell, -m)$ is opposite, because the magnitude of their waveform $|h_{\rm plus} + i * h_{\rm cross}|$ is identical, they have been plotted as one line, $(\ell, \pm m)$. This notation is continued throughout the rest of the paper. This plot thus establishes that there is indeed a visible and quantitative difference between waveforms with HOMs and without HOMs, as well as making it clear just how weak the HOMs can be. In this instance, the $Y_{3\pm2}$ mode is about two orders of magnitude smaller than the dominant mode, and subsequent HOMs only decrease further in strength.

B. Accounting for the Antenna Response

In order to make judgements about how much aLIGO would be able to distinguish between the full waveform and the dominant mode, we need to take into account the sky location of the merger relative to the detector. Using a built-in `GWpy` function, we are able to obtain the antenna response functions F_+ and $F_\times$ received by the

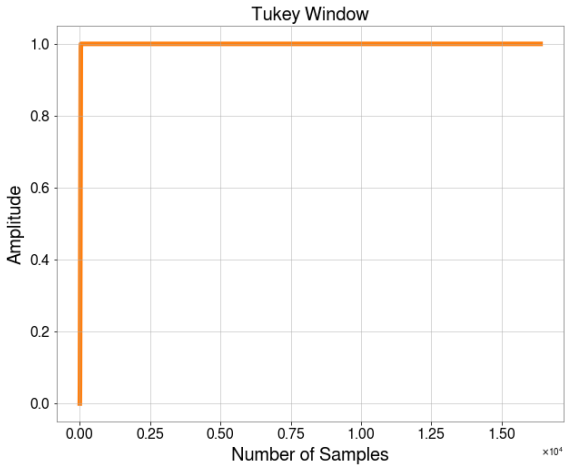

FIG. 4. The windowing function which is applied to the waveform data. This is a half-tukey window, meaning that there is no cut at the end of the time-domain waveform in order to preserve the data at the time of coalescence.

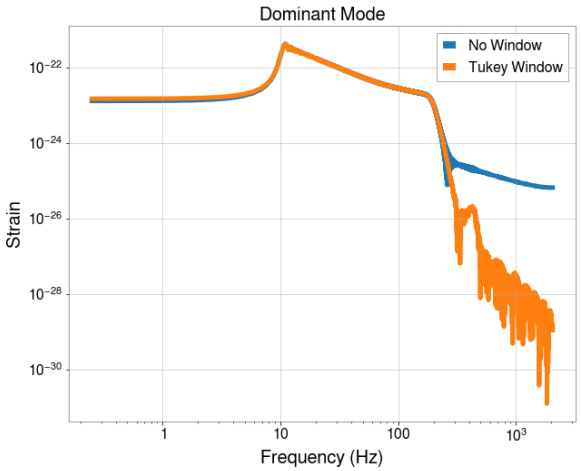

FIG. 5. The tukey window plotted in Figure 4 applied to the dominant mode data. The high-frequency Gibbs noise at the beginning of the waveform in the time-domain is drastically reduced, as expected.

detector. With Equation 6 below, we can thus obtain the strain observed by the detector [17].

$$h(t) = F_+(\alpha, \delta, \psi, t)h_+(t) + F_\times(\alpha, \delta, \psi, t)h_\times(t) \qquad (6)$$

Here, α refers to the RA, δ to the DEC, ψ to the polarization, and t the time of the merger. Because we are only concerned with relative comparisons between the two waveforms, we can simply take all of these values to be zero. The resulting observed signal is plotted in Figure 3, where the incoming plus and cross polarizations are plotted in blue and orange, respectively.

C. Refining the Data

Having visualized each of the modes in the time domain, we can now plot the HOMs as a function of frequency. First, we must ensure that each of the waveforms has the same duration of 4 seconds in order to make computing the overlap integral more uniform. To do this, we simply zeropad waveforms that are too short, and shorten waveforms that are too long. In the latter case, we cut data from the beginning of the signal so as not to interfere with the merger, where HOMs will reveal themselves.

After zeropadding, we must apply a windowing function to the data before performing a Fourier Transform in order to prevent nonphysical noise at low frequencies $\lesssim 10$ Hz and high frequencies $\gtrsim 500$ Hz. This is a phenomenon caused by Gibbs noise, whereby the Fourier Transform of a piece-wise function results in a ringing artifact at the point of discontinuity. Because the numerical relativity waveforms arbitrarily start at some time $t = 0$, the ringing artifact caused by this abrupt start will become visible as high-frequency noise in the Fourier Transform. To prevent this, we apply a half-Tukey window function to the data. As described by Equation 7 below, this is a variation on the classic Tukey window wherein there is only a cut at the beginning of the time-domain waveform, rather than at both ends, in order to target this Gibbs noise. Here, α is a constant which determines the width of each region of the Tukey window, and n is the number of samples.

$$w[n] = \begin{cases} \frac{1}{2}\left[1 + \cos\left(\pi\left(\frac{2n}{\alpha N} - 1\right)\right)\right] & 0 \le n < \frac{\alpha N}{2} \\ 1 & \frac{\alpha N}{2} \le n \le N \end{cases} \qquad (7)$$

Choosing a width of 40 samples for the first region in the Tukey window, Figure 4 plots this modified half-Tukey window as a function of the number of samples, and Figure 5 plots the Fourier Transform of the dominant mode with and without the Tukey window applied. The former case clearly has comparatively reduced noise in the high-frequency regime. It should also be noted that the decrease in strain at the beginning of this plot is purely an artifact of the artificial start time of the data, as in reality a merger would indefinitely increase in amplitude for lower frequencies.

D. Examining the Frequency Domain

Using this method of zeropadding and applying a window function to the data, we can finally Fourier Transform the data into the frequency domain. With this, we are able to plot the waveform for each mode, the dominant mode, and the sum of all modes against the total noise, obtained from aLIGO's updated design curve in

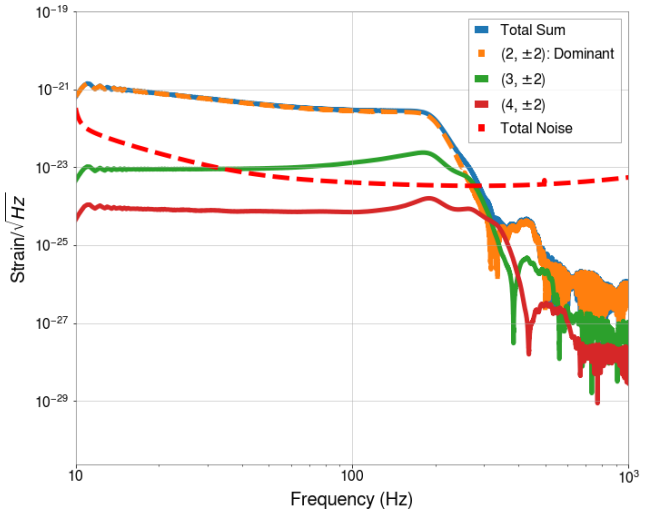

FIG. 6. The Fourier Transform of the simulation data plotted in Figure 2. In red is the LIGO design curve, and plotted in blue is the full waveform summing up all modes associated with this event. A half-Tukey window, described by Equation 7 has been applied to the data.

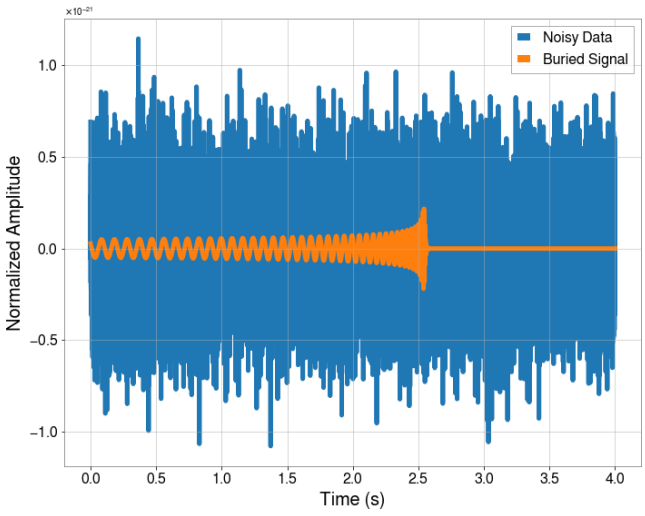

FIG. 8. An example of a full gravitational waveform signal, plotted in orange, hidden in noisy data, plotted in blue. This signal uses a numerical relativity surrogate model waveform with the input parameters listed in Table I, except for distance to the source merger, which is 4000 Mpc.

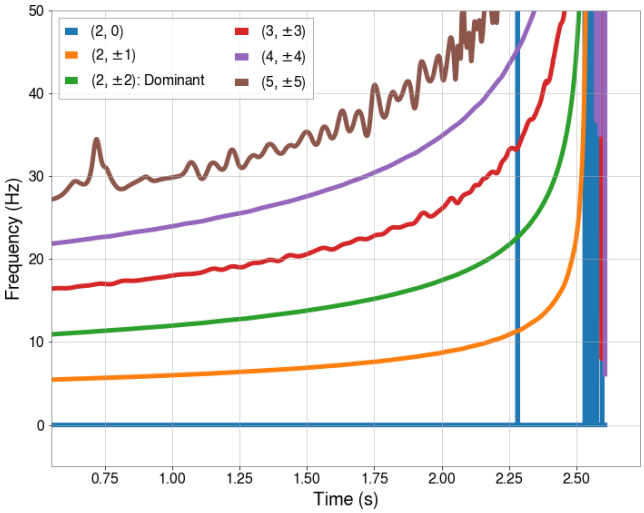

FIG. 7. This figure plots the derivative of the phase, or the instantaneous frequency of each waveform HOM component. The frequency peaks, as expected, at the time of coalescence.

Figure 1 (LIGO Scientific Collaboration). To do so, we must multiply the strain of the Fourier Transform plot by the square root of the frequency along the x-axis in order to match the units of this design curve. Doing so results in Figure 6, where the total noise serves as the Amplitude Spectral Density (ASD). It should be noted that the "humps" visible in the total sum at about 200-400 Hz are due to the underlying HOMs. This shows that there are clear differences between each of the HOMs, the dominant mode, and the full waveform. However, it is important to note that the total noise curve depicted in Figure 1 is an idealization of the noise curve. Noise, by definition, is random in time, but because the PSD is an average of many noise realizations, it is constant in the frequency domain. In order to find the optimal range of parameters in a more realistic fashion, we will need to work in the time domain of the noise. An example of what aLIGO's data might look like is illustrated in Figure 8, where the full GW signal is visibly buried in the noise.

Plotting these three curves together thus reveals the full range of frequencies in which the detectors can actually observe HOMs, as well as illustrating the delicate balance which exists between total merger mass, orbital orientation, and spin. A lower total mass increases the frequency of the merger and shifts the strain amplitude to the right, while the strain amplitude increases as the merger becomes more face-on. Adding spin will complicate this even further, as a merger might also precess about its orbital plane, and thus the observer's viewing angle with respect to the line of sight [18]. The effect of this precession on the observed waveform is better seen edge-on rather than face-on, but strain amplitudes are highest for face-on systems.

Finally, we plot the waveform's instantaneous peak frequency as a function of time, as depicted in Figure 7. Because we have chosen to plot only modes where $\ell = m$ we can easily see that the instantaneous frequency f scales with m such that $f_1/f_2 = m_1/m_2$. We have also zoomed in so that the beginning and end of the waveform is not depicted. In the full waveform, the instantaneous frequency fluctuates very heavily in the beginning due to noisy data, stabilizes for the most part, and then fluctuates heavily until it reaches peak frequency during coa-

lescence. This instantaneous frequency is the derivative of the phase, which monotonically decreases for all modes aside from the $m = 0$ mode, which do not oscillate. The maximum peak frequency for any individual mode depends on the total mass M, which is 100 $M_\odot$ in this plot, as well as the value of $|m|$.

E. Calculations

Now that we are able to visualize the waveform with and without HOMs, we compute the optimal SNR as a function of total merger mass, mass ratio, spin, and orbital orientation angle with respect to the observer's line of sight. More quantitatively, we compute the overlap integral $\mathcal{O}$ between the dominant Y_{22} mode and waveform with HOMs in order to find where the overlap is smallest. Because an overlap integral is essentially an inner product, if h_1 and h_2 are identical, then $\mathcal{O}$ will be equal to 1. The less they have in common, the smaller $\mathcal{O}$ is, indicating that the full signal with HOMs will be distinguishable from the dominant mode. The overlap integral is shown in Equation 8 below, where $h_1(f)$ and $h_2(f)$ are the waveform with and without HOMs, and PSD is the Power Spectral Density, referring to the square of the total design noise curve depicted in Figure 1:

$$\mathrm{PSD} = \mathrm{ASD}^2 \tag{8a}$$

$$\langle h_1|h_2\rangle = \int df \frac{h_1(f)\, h_2^*(f)}{\mathrm{PSD}(f)} \tag{8b}$$

$$\hat{h}_1 = \frac{h_1}{\sqrt{\langle h_1|h_1\rangle}} \tag{8c}$$

$$\mathcal{O} = \frac{\langle h_1|h_2\rangle}{\sqrt{\langle h_1|h_1\rangle\, \langle h_2|h_2\rangle}} = \left\langle \hat{h}_1|\hat{h}_2 \right\rangle \tag{8d}$$

In order to take into account how realistic a detection is, we calculate the value of the effective luminosity distance, d_L. This number is a measure of the furthest away a source merger can be in order for aLIGO to detect a difference in SNR between waveforms with and without HOMs of at least 1. This relation is described by Equation 9 below, where ΔSNR scales as $1/d_L$:

$$1 \leq \Delta\mathrm{SNR} \tag{9}$$

In order to obtain a value for the luminosity distance d_L in units of MPc, this SNR is computed at a distance of 1 Mpc, as defined by Equations 10a and 10b below:

$$\overline{\mathrm{SNR}}_1 = \frac{\langle h_{1\mathrm{Mpc}}|h_1\rangle}{\sqrt{\langle h_1|h_1\rangle}} = \left\langle h_{1\mathrm{Mpc}}|\hat{h}_1 \right\rangle \tag{10a}$$

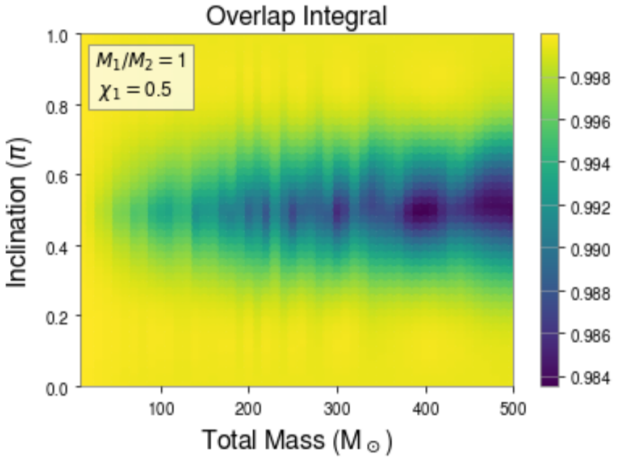

FIG. 9. The overlap integral computed for a range of masses from 1 to 500 $M_\odot$ and inclination angle θ from 0 to π. The mass ratio q has been fixed to 1 and the aligned spin of the larger mass component $\chi_{1,z}$ to 0.5.

$$\overline{\mathrm{SNR}}_2 = \frac{\langle h_{1\mathrm{Mpc}}|h_2\rangle}{\sqrt{\langle h_2|h_2\rangle}} = \left\langle h_{1\mathrm{Mpc}}|\hat{h}_2 \right\rangle \tag{10b}$$

Here, $\overline{\mathrm{SNR}}_1$ refers to the SNR signal of the waveform with HOMs $\hat{\mathrm{SNR}}_1$, while $\overline{\mathrm{SNR}}_2$ refers to the SNR signal of the waveform with just the dominant mode. Following this definition, as well as the notation used in Equation 8c, each respective SNR can essentially be redefined an inner product between the signal found in the data at 1 Mpc, $h_{1\mathrm{Mpc}}$, and the model waveform, either h_1 or h_2.

Using this definition of SNR, the effective luminosity distance can thus be described by Equations 11a and 11b below, where $\overline{\mathrm{SNR}}_1$ represents the SNR of the waveform with HOMs, and $\overline{\mathrm{SNR}}_2$ represents the SNR of the dominant mode waveform.

$$1 \leq \frac{\overline{\mathrm{SNR}}_1}{d_L} - \frac{\overline{\mathrm{SNR}}_2}{d_L} = \frac{1}{d_L}(\overline{\mathrm{SNR}}_1 - \overline{\mathrm{SNR}}_2) \tag{11a}$$

$$d_L \leq \overline{\mathrm{SNR}}_1 - \overline{\mathrm{SNR}}_2 \tag{11b}$$

IV. RESULTS

Now we are able to compute the overlap integral and luminosity distance for a range of initial parameters. To do so in a comprehensible and intelligible manner, we reduce the parameter space as much as possible by focusing on four variables exclusively: total mass M, mass ratio $q = m_1/m_2$, where $m_1 > m_2$, inclination angle θ, and the aligned spin component of the larger mass $\chi_{1,z}$. To compute how the overlap integral behaves in relation to

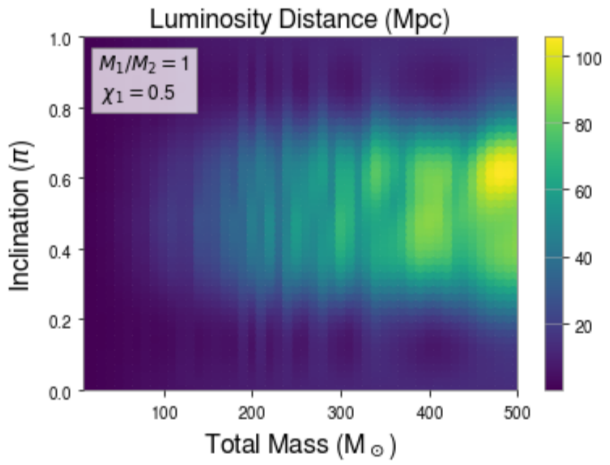

FIG. 10. The luminosity distance computed in Mpc for a range of masses from 1 to 500 $M_\odot$ and inclination angle θ from 0 to π. The mass ratio q has been fixed to 1 and the aligned spin of the larger mass component $\chi_{1,z}$ to 0.5.

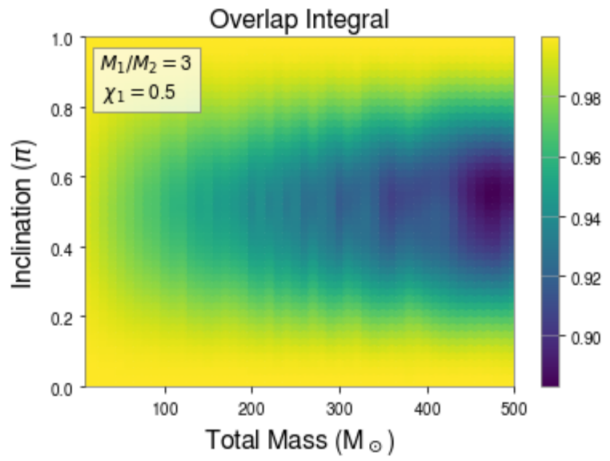

FIG. 11. The overlap integral computed for a range of masses from 1 to 500 $M_\odot$ and inclination angle θ from 0 to π. The mass ratio q has been fixed to 3 and the aligned spin of the larger mass component $\chi_{1,z}$ to 0.5.

these four parameters, we fix two of these parameters at a time and calculate the integral over 10 to 1000 Hz for a range of values within the other two parameters.

Fixing the mass ratio q and aligned spin $\chi_{1,z}$ thus produces the plots depicted in Figures 9 through 12. Fixing the total mass M and inclination angle θ instead produces the plot depicted in Figures 13 and 14. Finally, fixing the aligned spin $\chi_{1,z}$ and inclination angle θ produces the plots depicted in Figures 15 and 16.

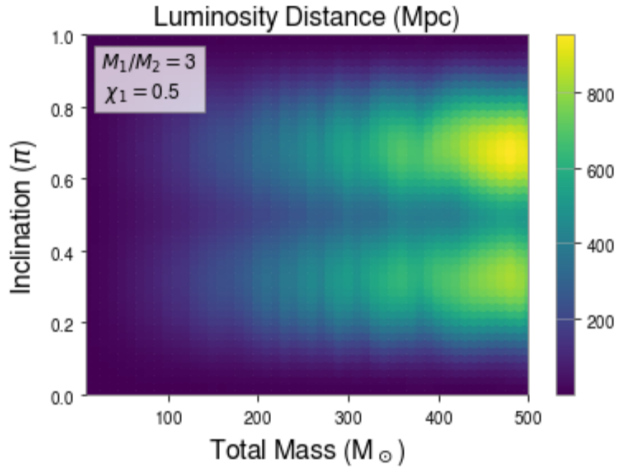

FIG. 12. The luminosity distance computed in Mpc for a range of masses from 1 to 500 $M_\odot$ and inclination angle θ from 0 to π. The mass ratio q has been fixed to 3 and the aligned spin of the larger mass component $\chi_{1,z}$ to 0.5.

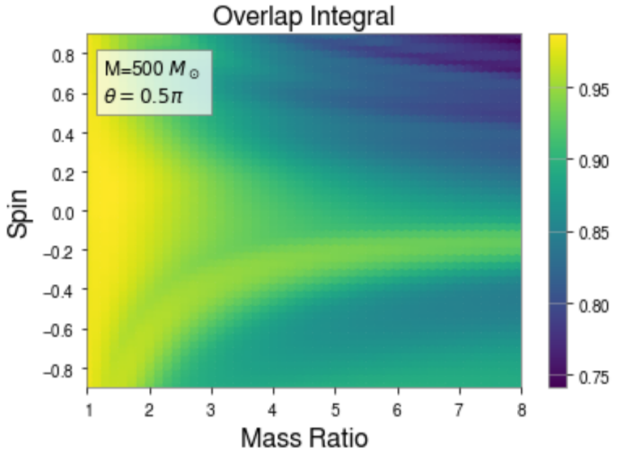

FIG. 13. The overlap integral computed for a range of mass ratios q from 1 to 8 and aligned spin of the larger mass component $\chi_{1,z}$ from -0.99 to 0.99. The total mass M has been fixed to 500 $M_\odot$ and the inclination angle θ to 0.5π.

V. CONCLUSIONS

The overlap integral informs us as to which HOMs are statistically significant and which are negligible. Experimenting with different masses and spins visually guides us to which combination is optimal, allowing us to gain an intuition for the SNR. The luminosity distance hones in on this and shows us how close a source merger must be in order for us to distinguish between a waveform with and without HOMs. Examining Figures 9 through 15 with this in mind, we can see some relations emerge.

Figure 9 holds q constant at 1 and $\chi_{1,z}$ constant at 0.5.

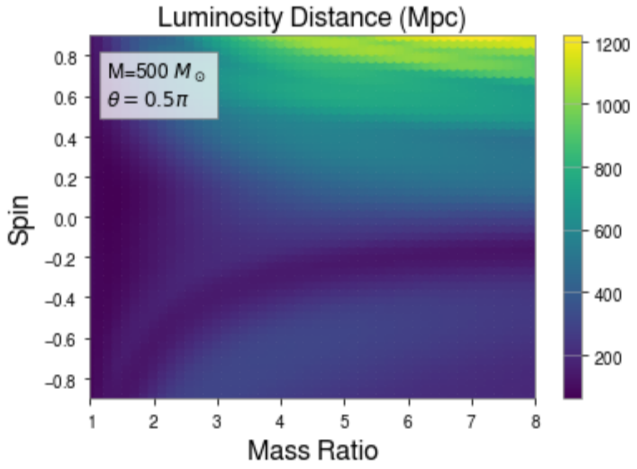

FIG. 14. The luminosity distance computed in Mpc for a range of mass ratios q from 1 to 8 and aligned spin of the larger mass component $\chi_{1,z}$ from -0.99 to 0.99. The total mass M has been fixed to 500 $M_\odot$ and the inclination angle θ to 0.5π.

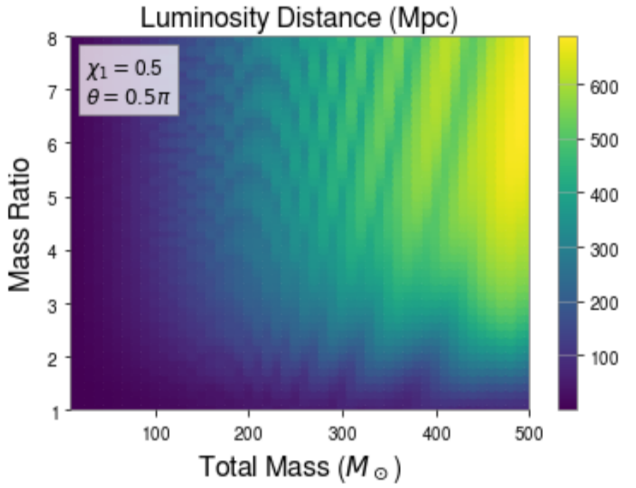

FIG. 16. The luminosity distance computed in Mpc for a range of masses from 1 to 500 $M_\odot$ and mass ratios q from 1 to 8. The aligned spin of the larger mass component $\chi_{1,z}$ has been fixed to 0.5 and the inclination angle θ to 0.5π.

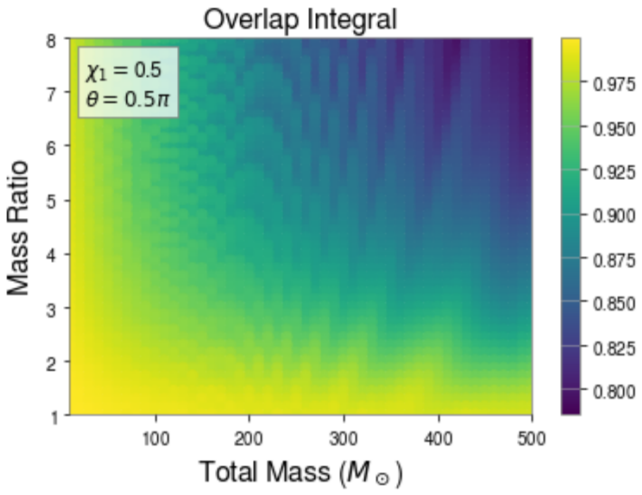

FIG. 15. The overlap integral computed for a range of masses from 1 to 500 $M_\odot$ and mass ratios q from 1 to 8. The aligned spin of the larger mass component $\chi_{1,z}$ has been fixed to 0.5 and the inclination angle θ to 0.5π.

The overlap integral appears to peak for as large a total mass M as possible. The luminosity distance in Figure 10 appears to tell the same story. However, it is important to keep in mind that the assumptions constraining these conclusions. First of all, the highest mass that is considered is 500 $M_\odot$. However, when the total mass exceeds ≈ 100 $M_\odot$, aLIGO is unable to detect these events because BBH mergers of this size do not exist, and even if they did, they would merge at frequencies below the sensitive band of the aLIGO detectors. Thus, Figures 9 and 10 inform us that in order to distinguish HOMs, it is optimal for the total mass to be as high as possible within these limits.

However, the relation to the inclination angle θ appears to be a bit more complicated: in Figure 9, the overlap integral peaks for an inclination angle θ of $\sim 0.5\pi$, but in Figure 10, the luminosity distance appears to favor a slightly higher θ of $\sim 0.7\pi$. Increasing the mass ratio q to 3 reveals a further complication: although the overlap integral seems to favor the same inclination angle of $\sim 0.5\pi$, as depicted in Figure 11, the luminosity distance does not. Figure 12 shows that the luminosity distance decreases at that inclination angle, meaning that a source needs to be closer in order to be able to distinguish HOMs. For a larger luminosity distance, an inclination angle of $\sim 0.75\pi$ and to a lesser extent, $\sim 0.25\pi$, seem to optimize the difference in SNR. Because this change in optimal inclination angle is spurred on by the shift in mass ratio, this seems to suggest that inclination angle has a more complex relationship with luminosity distance and the overlap integral than does the total mass. It thus appears that the optimal inclination angle depends on which HOMs are most dominant at a certain mass ratio, as unequal mass systems will have different combinations of HOMs.

The relationship between the overlap integral, luminosity distance, and the aligned spin of the larger mass component $\chi_{1,z}$ appears to be more straightforward. When total mass M and inclination angle θ is fixed at 0.5π in Figures 13 and 14, the overlap integral is lowest, and the luminosity distance highest, for as large and positive a spin as possible. The overlap integral and luminosity distance are similarly optimized for as large a mass ratio as possible. This can be seen even more clearly in Figures 15 and 16, which fix the spin $\chi_{1,z}$ at 0.5 and the

inclination angle θ at 0.5π. The preference for high total mass can also be seen here.

VI. FUTURE WORK

These results shed light into the limit of GR in the strong-field, highly dynamical regime. It should be noted that these results do not explore parameter space in its entirety, and only represent slices of data at fixed parameters. For a more comprehensive review, we would need to perform a full Bayesian model selection analysis. There is also room to explore more fully when exactly the overlap integral begins to increase (and the luminosity distance decrease) for extremely high mass systems, as eventually they will fall of the aLIGO updated design curve. We also need to better understand what parameters the optimal inclination angle θ depends on, and why, as the physics is currently not fully explored. Finally, we would still need to look into how precessing systems with non-aligned spins behave, as we only examined non-precessing BBH mergers.

ACKNOWLEDGEMENTS

I would like to thank Alan Weinstein for serving as my research advisor on this project, as well as Liting Xiao and Jonah Kanner for their guidance. I would also like to thank the Caltech Student Faculty Program (SFP) for organizing the LIGO SURF program. Finally, I would like to thank the National Science Foundation (NSF) for their funding, as well as the Rouse Family for their financial support with the Carl A. Rouse Memorial Fellowship.

[1] Einstein A. Approximative Integration of the Field Equations of Gravitation. Sitzungsber Preuss Akad Wiss Berlin (Math Phys). 1916;1916:688–696.

[2] Einstein A. Über Gravitationswellen. Sitzungsber Preuss Akad Wiss Berlin (Math Phys). 1918;1918:154–167.

[3] Abbott BP, Abbott R, Abbott TD, Abernathy MR, Acernese F, Ackley K, et al. Observation of Gravitational Waves from a Binary Black Hole Merger. Phys Rev Lett. 2016 Feb;116:061102. Available from: https://link.aps.org/doi/10.1103/PhysRevLett.116.061102.

[4] The LIGO Scientific Collaboration, the Virgo Collaboration, Abbott BP, Abbott R, Abbott TD, Abraham S, et al. GWTC-1: A Gravitational-Wave Transient Catalog of Compact Binary Mergers Observed by LIGO and Virgo during the First and Second Observing Runs. arXiv e-prints. 2018 Nov;p. arXiv:1811.12907.

[5] Acernese F, Agathos M, Agatsuma K, Aisa D, Allemandou N, Allocca A, et al. Advanced Virgo: a second-generation interferometric gravitational wave detector. Classical and Quantum Gravity. 2015 Jan;32(2):024001.

[6] Abbott BP, Abbott R, Adhikari R, Ajith P, Allen B, Allen G, et al. LIGO: the Laser Interferometer Gravitational-Wave Observatory. Reports on Progress in Physics. 2009 Jul;72(7):076901.

[7] Turpin D, Wu C, Han XH, Xin LP, Antier S, Leroy N, et al. The mini-GWAC optical follow-up of the gravitational wave alerts: results from the O2 campaign and prospects for the upcoming O3 run. arXiv e-prints. 2019 Feb;p. arXiv:1902.08476.

[8] Cai RG, Cao Z, Guo ZK, Wang SJ, Yang T. The Gravitational-Wave Physics. arXiv e-prints. 2017 Mar;p. arXiv:1703.00187.

[9] Babak S, Balasubramanian R, Churches D, Cokelaer T, Sathyaprakash BS. A template bank to search for gravitational waves from inspiralling compact binaries: I. Physical models. Classical and Quantum Gravity. 2006 Sep;23(18):5477–5504.

[10] Payne E, Talbot C, Thrane E. Higher order gravitational-wave modes with likelihood reweighting. arXiv e-prints. 2019 May;p. arXiv:1905.05477.

[11] Kumar P, Blackman J, Field SE, Scheel M, Galley CR, Boyle M, et al. Constraining the parameters of GW150914 and GW170104 with numerical relativity surrogates. Phys. Rev. D. 2019 Jun;99(12):124005.

[12] Varma V, Field SE, Scheel MA, Blackman J, Kidder LE, Pfeiffer HP. Surrogate model of hybridized numerical relativity binary black hole waveforms. Physical Review D. 2019 Mar;99(6). Available from: http://dx.doi.org/10.1103/PhysRevD.99.064045.

[13] Centrella JM. What can we learn about cosmic structure from gravitational waves? In: Holt SH, Reynolds CS, editors. The Emergence of Cosmic Structure. vol. 666 of American Institute of Physics Conference Series; 2003. p. 337–346.

[14] Eshky A. Bayesian Methods of Parameter Estimation Aciel Eshky; 2009. .

[15] Thrane E, Talbot C. An introduction to Bayesian inference in gravitational-wave astronomy: Parameter estimation, model selection, and hierarchical models. . 2019 Mar;36:e010.

[16] Macleod D, Urban AL, Coughlin S, Massinger T, paulaltin, Areeda J, et al.. gwpy/gwpy: 0.14.2; 2019. Available from: https://doi.org/10.5281/zenodo.2603187.

[17] Van Den Broeck C, Sengupta AS. Binary black hole spectroscopy. Classical and Quantum Gravity. 2007 Mar;24(5):1089–1113.

[18] Dietrich T, Bernuzzi S, Brügmann B, Ujevic M, Tichy W. Numerical relativity simulations of precessing binary neutron star mergers. Phys. Rev. D. 2018 Mar;97(6):064002.